Plasmoelectronic properties of self-assembled gold nanoparticles: impedance spectroscopy experiments combined with numerical simulations

Louis Merle, Adnen Mlayah, J. Grisolia

Plasmo-electronic properties of self-assembled gold nanoparticles: impedance spectroscopy experiments combined with numerical simulations

LOUIS MERLE[1], ADNEN MLAYAH[2,3] AND JÉRÉMIE GRISOLIA[*1]

[1] *LPCNO, Université de Toulouse, INSA, CNRS, UPS, 135 Avenue de Rangueil, Toulouse 31077, France*
[2] *CEMES, Université de Toulouse, CEMES-CNRS, 29 rue Jeanne Marvig, Toulouse 31055, France*
[3] *LAAS, Université de Toulouse, CNRS, UPS, 7 avenue du Colonel Roche, Toulouse 31031, France*
[*] *jeremie.grisolia@insa-toulouse.fr*

Abstract: Plasmo-electronics is a fast developing field driven by the combination of charge transport and surface plasmons in metal nanostructures. In this paper, we report on theoretical and experimental investigations of the plasmoelectronic properties of self-assembled monolayers of colloidal gold nanoparticles. A local plasmonic-electronic nano-junction is introduced, as the fundamental component of a meso-scale electrical network, and serves as the beginning point for the development of a multi-scale modeling strategy. The Inter-particle charge tunneling and accumulation account for the dynamical charge transport; the plasmonic properties are implemented at the nanoscale using electro-dynamic calculations based on the discrete dipole approximation (DDA) method. The electric characteristics of the macroscopic nanoparticle network are calculated using a numerical resolution of the current-bias equations based on Kirchhoff's laws. Disorder effects due to size and position fluctuations of the nanoparticles within the network as well as dislocations and point defects in their spatial arrangement are taken into account. The effects of light excitation intensity and wavelength on the nano-junction photo-conductance and on the macroscopic photo-resistance of the nanoparticle network are addressed. In particular, plasmo-electronic conduction paths are extracted from the coupled DDA-Kirchhoff numerical simulations and their statistical distribution is investigated as well as their dependence on path length. The theoretical results are compared with impedance spectroscopy measurements performed under optical excitation. We found a good agreement between the predicted impedance Nyquist plots and resonance properties, and the measurements. In particular, we were able to estimate the surface plasmon assisted photo-electric conversion coefficient involving first neighbor nanoparticles. We found that the photo-conductance of a single nano-junction formed by a dimer of nearly touching nanoparticles is around 18 $nS.W^{-1}.cm^2$ under resonant plasmonic excitation. The presented work provides insight into the photo-induced charge transport in self-assembled nanoparticle networks and opens the route to novel applications in the field of plasmo-electronics.

1. Introduction

The driving force behind the development of plasmoelectronics is the link between charge transport and surface plasmons in metal nanostructures [1]–[5]. It has been shown that charging metal nanoparticles can alter their plasmonic response, and vice versa, that surface plasmon excitation of a nanoparticle assembly can modify

macroscopic fluxes of charges [6]–[8]. In particular, a rise or a decrease of conductance, under optical excitation tuned to the nanoparticles surface plasmon resonance, has been pointed out [6], [9], [10]. In this situation, it had been found that negatively charged ligands act as charge traps lowering the free carrier density and resulting in a negative photo-conductance. However, since positive photo-conductance with charged ligands has also been discovered, this view has been vividly contested in the literature [11]–[13]. Additionally, the ligand molecules' ability to impose a tunnel barrier between two adjacent nanoparticles, regardless of their charge state, determines whether the macroscopic electrical properties of the nanoparticle assemblies behave like a metal or an insulator [14]. Moreover, despite the fact that these NPs assemblies are granular in form, that is, made up of conductive and insulating regions, most published investigations to date have concentrated on the analysis of the resistance properties, only [6] [9]–[11], [13]–[21]. The capacitive properties have only been briefly discussed in a few papers [12], [22]. In this respect, we have previously demonstrated [12], that both resistive and capacitive characteristics are complementary and can be used to further understanding the charge transport properties of self-assembled nanoparticle networks. Indeed, the macroscopic electrical characteristics of self-assembled NPs were experimentally investigated using impedance spectroscopy and were modeled using a bottom-up approach in which local interconnected nano-junction circuits are introduced as building blocks of a macroscopic electrical circuit to describe the charge transport properties of the nanoparticle self-assembly (Figure 2). However, the photo-induced effects were accounted only at the macroscopic level, which provided a first attempt to the modeling of the plasmonic induced photo-conductance in self-assembled gold nanoparticle networks and the macroscopic conversion efficiency of the electromagnetic energy into electric current has been estimated.

In this paper, we focus on the conversion of light into electrical current in self-assembled plasmonic NPs networks. This phenomenon is quite complex and involves several interaction steps between elementary excitations (plasmons, electron-hole pairs, phonons), but it is still poorly understood in terms of the relationship between local opto-electronic properties at the nanoparticle scale and the macroscopic electrical characteristics of the nanoparticle self-assembly. We demonstrate that utilizing numerical simulations combined with impedance spectroscopy measurements, it is possible to connect the macro-scopic and the nano-scopic opto-electronic properties of metal NPs assemblies. To account for the photo-induced charge carriers generation and transport, a local positive photoconductance is introduced at the nano-scale. The current passing through the nanoparticle assembly, including its optical component, is determined by implementing electrodynamic calculations into Kirchhoff's laws. This method enables the definition of a macroscopic photo-conductance. The theoretical results are discussed in terms of plasmo-electronic properties of the nanoparticle self-assembly and are compared to impedance spectroscopy measurements carried out under optical excitation of the plasmonic resonance of the nanoparticles. In this way we are able to assess the efficiency of the plasmonic assisted light-to-current conversion at the nanoscopic level. Such a physical quantity is very difficult to determine including in near-field based optical spectroscopy techniques.

2. Experimental and numerical details:

2.1 - Chemical synthesis and sample preparation:

The chemical synthesis procedure is described in details elsewhere [22], [23]. Briefly, gold nanoparticles stabilized with dodecanethiol (C_{12}) organic ligands (1.2nm length) were synthesized with the protocol described by Zheng et al. [24]. The average size of the nanoparticles is $7 \pm 0.7\,nm$ determined by transmission electronic microscopy (TEM). On the other hand, interdigitated gold electrodes were patterned on a 125 µm thick polyimide (Upilex) film using laser lithography and a 50 nm thick Au layer was deposited over the entire surface by IBS-E ion beam sputtering. After lift-off, a 1 mm² device consisting in 50 pairs of inter-digitated 5 µm wide electrodes separated by 5 µm is obtained and connected to external gold electrodes (Figure 1a). Gold NPs from the colloidal solution were deposited on the device using the ethylene glycol drop casting method described elsewhere (Figure 1b) [22]. This technique allows to obtain a quite uniform and homogeneous monolayer of self-assembled nanoparticles well ordered in a hexagonal lattice network on a macroscopic scale (1 mm^2) (Figure 1).

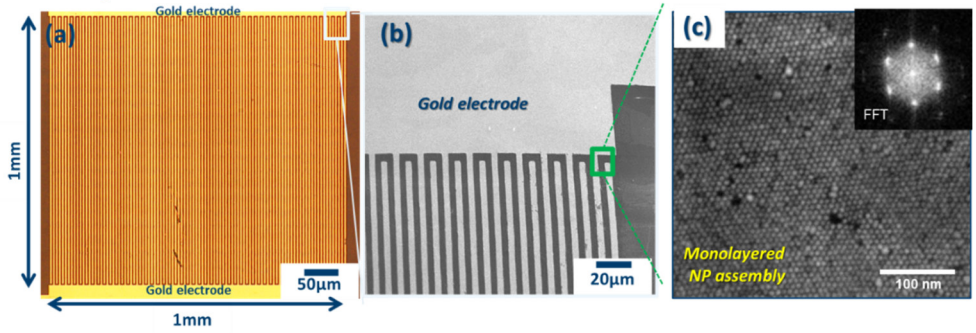

Figure 1 : (a) Optical image showing a 1mmx1mm device formed by 50 interdigited electrodes (b) Scanning electron microscopy (SEM) image of the interdigitated electrodes on top of which the NP assembly is formed, (c) High resolution SEM image of the active area showing a monolayer of 7 nm gold nanoparticles self-assembled in a hexagonal lattice network, as attested by the electron diffraction pattern in the inset.

2.2 - Impedance spectroscopy under optical excitation:

Impedance spectroscopy measurements were performed at room temperature using a Keysight impedance analyzer EA4990A, in the 20Hz-5MHz frequency range with a 500mV AC voltage. The set-up is equipped with an optical fiber located above the sample which allows to shine laser light on the 1mm² entire active area (Figure 1a). The optical fiber is connected to three laser diodes, operating at λ = 405, 532 and 640 nm wavelengths and up to W/cm^2 intensity.

3. Plasmoelectronic modeling:

The approach developed in this work is based on numerical simulations of the dynamical charge transport properties of a network composed of inter-connected electric nano-circuits building blocks (Figure 2).

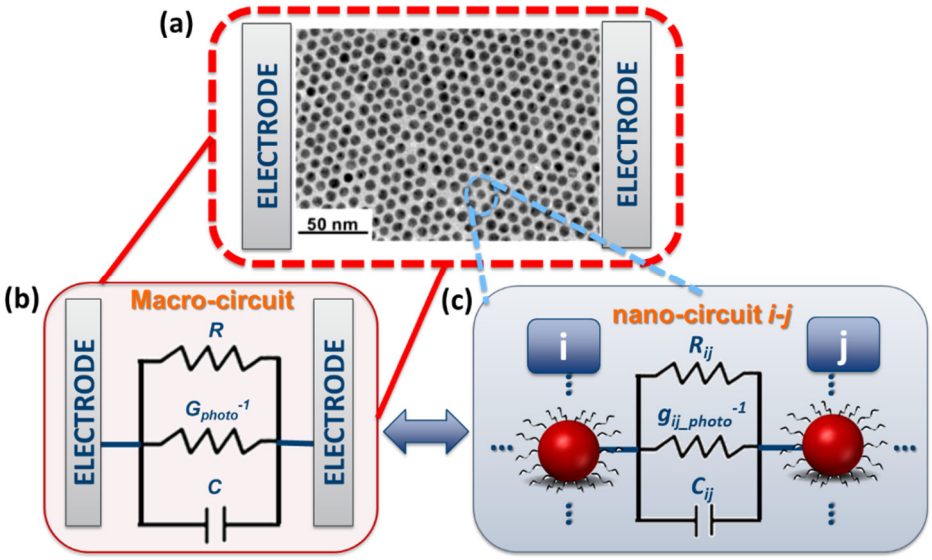

Figure 2: (a) Transmission Electron Microscopy image of a ca. 220nm x 150nm region of the NP assembly with schematic contact electrodes, (b) electrical circuit formed by parallel resistance R, capacitor C and photo-resistance G_{photo}^{-1} describing the charge transport across the network formed by the inter-connected nano-junctions (c). Each nano-junction, formed by a pair of first neighbor nanoparticles, consists in parallel inter-particle tunneling resistance R_{ij}, capacitor C_{ij} and photo-resistance $g_{ij\_photo}^{-1}$.

Each nano-junction is an electrical connexion between first neighbor nanoparticles (labeled *i* and *j*) and consists in parallel inter-particle resistance R_{ij}, capacitor C_{ij} and photo-resistance $g_{ij\_photo}^{-1}$ (Figure 2c). Calculations were performed for a single layer of spherical gold NPs. The sizes and positions of the nanoparticles, as well as the inter-particle gap distances were extracted from a 100 nm x 100 nm area of the transmission electron microscopy (TEM) images (Figure 2a). The histogram of interparticle distances in Figure ESI 1b shows that the average inter-particle gap separation is around 2.8 nm which is slightly larger than twice the dodecanethiol molecule length (1.2 nm). This indicates that disorder due to size and position fluctuations, to point defects (nanoparticle vacancies) and to dislocations and misfits in the nanoparticle network are present. Figure ESI 1a depicts the 100 nm x 100 nm nanoparticle region that serves as our model network for the computer simulations. In this way, the actual spatial arrangement of the nanoparticles are taken into account in the calculations and in the comparison with the experimental data.

Each *(i,j)* pair of nanoparticles located at positions (r_i, r_j) of the 2D network gives rise to a parallel electrical nano-junction (Figure 2c) with admittance:

Eq. 1 $$\chi_{ij} = 1/R_{ij} + g_{ij\_photo} + jC_{ij}\omega$$

As shown in previous works [11], [14], [25], the quantum tunnelling resistance R_{ij} between first neighbour nanoparticles is given by:

Eq. 2 $$R_{ij} = R_0 . e^{\xi(v_{ij},T)}$$

where R_0 is the inter-particle tunnelling resistance at the touching limit, *i.e.* for vanishing inter-particle gap distance l_{ij}, ξ accounts for the charge tunnelling and for the Coulomb blockade effects and is given by ([11], [14], [25], [25]):

Eq. 3 $\xi = \beta l_{ij} - ln\left(g\left(E_c, T, V_{ij}\right)\right)$ *with* $g\left(E_c, T, V_{ij}\right) = \frac{1}{eV_{ij}}\left(-\frac{E_C - eV_{ij}}{1-e^{\left(E_C - eV_{ij}\right)/k_B T}} + \frac{E_C + eV_{ij}}{1-e^{\left(E_C + eV_{ij}\right)/k_B T}}\right)$

Where β is the tunnelling decay constant, E_C is the Coulomb charging energy, T the temperature and V_{ij} is the voltage between first neighbour nanoparticles i and j. In the following we use β = 5 nm^{-1} and E_C = 50meV ([11], [13]) to describe the tunneling resistance in the absence of optical excitation.

It is worth noting that the bias voltage applied to the nanoparticle network is of the order of volts leading to inter-particle voltage V_{ij} very small compared to Ec/e ~ 50mV. In addition $E_C > k_B T$ at room temperature. Using these two statements, Eq. 3 can be approximated by [27]:

Eq. 4 $$\xi \approx \beta l_{ij} + {E_c}/{k_B T}$$

Assuming spherical nanoparticles, the inter-particle capacitor C_{ij} is given by [22], [26]:

Eq. 5 $$C_{ij} = \pi\varepsilon\bar{d}_{ij}.ln\left(1 + \bar{d}_{ij}/l_{ij}\right)$$

Where $\bar{d}_{ij} = \left(d_i + d_j\right)/2$ is the mean diameter of the i and j nanoparticles and ε is the permittivity of the surrounding medium (*i.e.* of the ligand molecules in our case).

As shown experimentally by Mangold *et al.* [10], [17], Gauvin *et al.* [28], the macroscopic photo-conductance increases linearly with increasing laser intensity for low laser irradiation (below 7kW/cm^2). This is confirmed in our investigated nanoparticle networks as shown in Figure ESI 2. Based on this experimental finding, we introduce a local nanoscopic photoconductance:

Eq. 6 $$g_{ij\_photo}(\lambda) = k_{ij}(\lambda).I_{ij}(\lambda).e^{-E_C/k_B T}$$

Where $k_{ij}(\lambda)$ is a wavelength dependent local photo-conductance efficiency involving first neighbor nanoparticles and the surrounding ligands molecules. $I_{ij}(\lambda) = {F_{ij}}^2(\lambda)\, I_0$ is the local light intensity and $F_{ij}(\lambda) = |E_{ij}(\lambda)/E_0|$ is the electric field enhancement factor which accounts for the plasmonic resonance; $I_0 = |E_0|^2$ is the incident optical intensity.

In our approach, the light-to-current conversion mechanism is treated globally, *i.e.* as due to both the nanoparticle and its surrounding medium; indeed, the ligand molecules may also absorb light through HOMO-to-LUMO transitions and may thus participate to the photo-generation of electron-hole pairs. Therefore, we assume that $F_{ij}(\lambda)$ is the electric field enhancement factor in the gap region between i and j nanoparticles. The photo-generated charges flow across the nanoparticle network owing to quantum tunneling between first neighbor nanoparticles. The photo-conductance efficiency $k_{ij}(\lambda)$ depends on the optical wavelength because the tunneling process involves high energy photo-excited states (see Figure ESI 3), the so-called hot charge carriers. Therefore, we make the assumption that $k_{ij}(\lambda)$ takes the form :

Eq. 7 $$k_{ij}(\lambda) = k_0(\lambda).e^{-\beta(\lambda).l_{ij}}$$

Where $k_0(\lambda)$ is a wavelength-dependent photo-conductance efficiency in Siemens per unit of light intensity, which accounts for the photo-generation charge carriers at vanishing gap distance between two nanoparticles; and the exponential term describes their interparticle tunneling; $\beta_{hot}(\lambda) = \sqrt{2.m.(V_b - E(\lambda))/\hbar)}$ is the wave vector of the photo-generated hot electrons, in which, m = 0.28.m$_0$ is the carriers

electron effective mass [29], $E(\lambda)$ is the photon energy and $V_b = 4.16$ eV is the energy barrier height [29]. For example, at $\lambda = 532$ nm, $\beta_{hot} = 3.66\ nm^{-1}$ and is smaller than $\beta = 5\ nm^{-1}$ which conveys the idea that hot carriers can tunnel over larger distances than thermalized carriers (Figure ESI 3).

Calculations based on the Discrete Dipole Approximation (DDA) [30], [31] were performed in order to determine the plasmonic field enhancement $F_{ij}(\lambda)$. The nanoparticle self-assembly model is the 100 nmx100 nm area shown in Figure ESI 1a. The medium surrounding each nanoparticle is dodecanethiol (with optical index n=1.46).

Figure 3 shows maps of $F_{ij}(\lambda)$ calculated at three optical excitation wavelengths around the plasmonic resonance. These maps show that the electro-magnetic interactions between the NPs give rise to plasmonic hot spots in the gap regions between the nanoparticles. For the calculation of the local field intensity in Eq. 6, we consider the intensity enhancement $<F_{ij}^2(\lambda)>$ averaged over the gap distance between first neighbor nanoparticles (Figure 3d). $<F_{ij}^2(\lambda)>$ is around two orders of magnitudes for a 1 nm interparticle distance and decreases with increasing l_{ij} (Figure 3e) which confirm the origin of the plasmonic resonance as due to the near-field interaction between first neighbor nanoparticles.

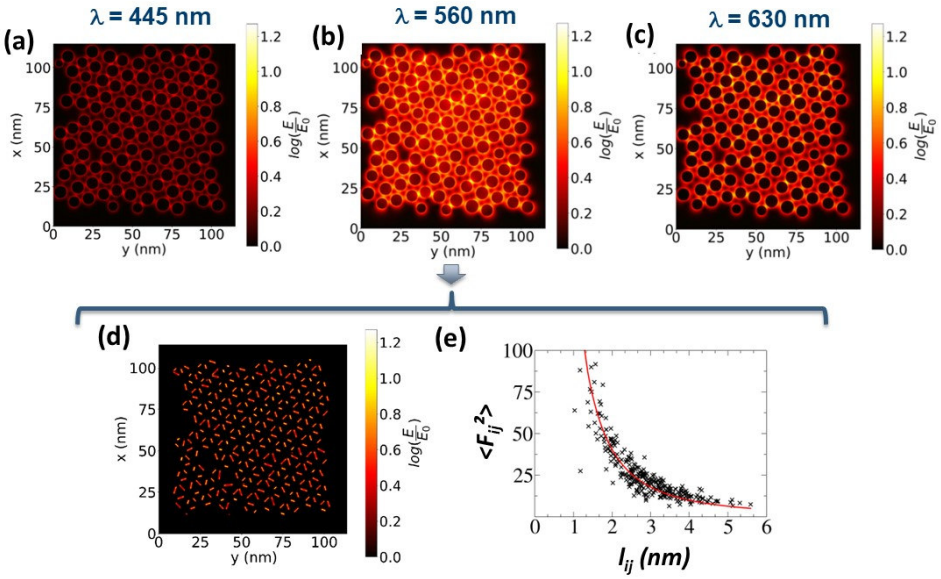

Figure 3 : Electric field intensity enhancement $F_{ij}(\lambda) = |E_{ij}(\lambda)/E_0|$ calculated using DDA simulations performed on a 100 nm x 100 nm nanoparticle assembly shown in Figure ESI 1a. Maps of $F_{ij}^{\ 2}$ calculated around the surface plasmon resonance at 445 nm (a), 560 nm (b) and 630 nm (c). The excitation wave is circularly polarized in the assembly plane, (d) Map of $<F_{ij}^2>$ *the* field intensity enhancement calculated at 560 nm and averaged over the gap distance between each pair of nanoparticles; (e) plot of $<F_{ij}^2>$ as a function of inter-particle distance l_{ij}.

The $<F_{ij}^2>$ calculated using the DDA numerical simulations are used in Eq. 6 to generate the local photoconductances.

The complex admittance matrix [Y] of the electrical network, formed by the interconnected nano-junctions, is constructed assuming that all first neighbor nanoparticles are located within a ring centered on the considered nanoparticle. The current flowing throughout the NP network is computed according to Kirchhoff's laws and by solving numerically the matrix equation[32]:

Eq. 8 $$[\boldsymbol{V}(\boldsymbol{\omega})] = [\boldsymbol{Y}(\boldsymbol{\omega})]^{-1}[\boldsymbol{I}(\boldsymbol{\omega})]$$

where $[\mathbf{V}(\boldsymbol{\omega})]$ and $[\mathbf{I}(\boldsymbol{\omega})]$ are, respectively, the voltage and the injected current vectors, and $[\boldsymbol{Y}(\boldsymbol{\omega})]$ is the complex admittance matrix of which non-diagonal and diagonal terms are, respectively, $\boldsymbol{Y_{ij}}(\boldsymbol{\omega}) = -\boldsymbol{\chi}_{ij}(\boldsymbol{\omega})$ for $i \neq j$ and $\boldsymbol{Y_{ii}}(\boldsymbol{\omega}) = \sum_j \boldsymbol{\chi}_{ij}(\boldsymbol{\omega})$; the latter being the total admittance connected to node i [33].

The overall admittance of the network is $\boldsymbol{Y_0^{-1}}(\boldsymbol{\omega}) = \boldsymbol{V_0}(\boldsymbol{\omega})/\boldsymbol{I_0}(\boldsymbol{\omega})$ where $\boldsymbol{V_0}(\boldsymbol{\omega})$ is the voltage vector at the collecting electrode and $I_0(\boldsymbol{\omega})$ is the injected current vector.

It is important to note that after the admittance $\chi_{ij}(\omega)$ (Eq. 1) of the local nano-junction is adjusted for the local photo-conductance $g_{ij\_photo}(\lambda)$ (Eq. 6), calculated using DDA simulations, and the matrix equation (Eq. 8) is numerically solved using Kirchhoff's laws, one obtains the overall conductance, capacitance, and photo-conductance of the nanoparticle assembly. The numerical simulations utilizing this strategy enable modeling of the plasmo-electronic properties of self-assembled metal nanoparticles and is, going forward, referred to as DDA-Kirchhoff's method.

4. Results and discussion:

4.1 Numerical simulations:

Figure 4 presents Nyquist plots (Figure 4a) and resonance curves of the imaginary part $-Z''(\omega)$ of the impedance calculated using DDA-Kirchhoff simulations. The parameters used in these simulations are R_0 = 80 kΩ (in Eq. 2) and k_0 = 18 nS.W^{-1}.cm² (in Eq. 7). The choice of these values will be discussed later.

All Nyquist plots have nearly a semicircle shape which is a characteristic feature of an equivalent circuit consisting in parallel resistance R, capacitor C and photo-resistance G_{photo}^{-1}.

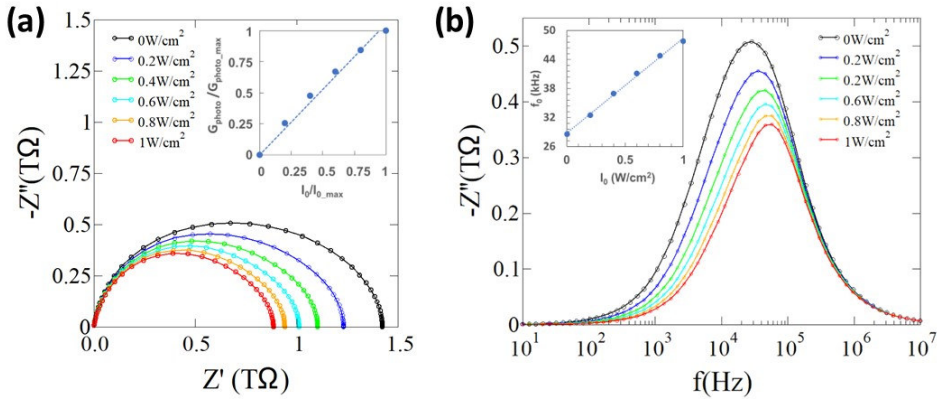

Figure 4 : DDA-Kirchhoff numerical calculations of the impedance of the network shown in Figure ESI 1a. (a) impedance Nyquist plots in the range 20 Hz-1 MHz, without and with optical excitation at 532 nm with intensity increasing from 0 to 1W/cm² (inset: normalized photoconductance as a function of normalized I_0). (b) Spectrum of the Imaginary part of the calculated impedance $-Z''(\omega)$ (inset: corresponding f_0 evolution as a function of laser intensity).

The frequency dependence of the impedance arises from the capacitance contribution only. At this step, R, C and G_{photo}^{-1} can be considered as mesoscopic quantities reflecting the electric and plasmo-electric properties of the 100 nm x 100 nm simulated network (Figure ESI 1a) formed by the interconnected nano-junctions. They are not macroscopic quantities yet, since the latter are related to the macroscopic properties of the samples (Figure 1) onto which impedance spectroscopy measurements were performed (see discussion below).

First, a clear decrease of the impedance with increasing intensity of the optical excitation can be observed in Figure 4a. This can be understood in terms of the equivalent circuit impedance $\frac{R}{1+RG_{photo}}$ formed by the parallel resistance and photo-resistance G_{photo}^{-1} in the low-frequency limit (values of $Z'(\omega)$ on the horizontal axis of Nyquist plots in Figure 4a). Nyquist plot calculated without light irradiation ($G_{photo} = 0$), gives $R = 1.4\,T\Omega$. With increasing optical excitation, G_{photo} increases and may dominate the resistive character of the circuit in the limit of strong irradiation intensity ($G_{photo} \gg R$). The inset of Figure 4a shows the values of G_{photo} deduced from the low-frequency limit of the Nyquist plots (Figure 4a).

Inset of Figure 4a shows that G_{photo} increases linearly from 0 to *c.a.* $0.4\,pS$ with irradiation intensity I_0 in agreement with the local photo-conductance model (Eq. 6) implemented at the nanoscale and with the experimental data (Figure ESI 2). Moreover, one can notice in Figure 4 that the Nyquist plots are not perfect semi-circles; they are depressed, *i.e.* the ratio between the maximum values of the imaginary and real parts of the impedance $-Z''_{max}/Z'_{max} < 0.5$. For instance, without optical excitation (black dots in Figure 4a) $-\frac{Z''_{max}}{Z'_{max}} = 0.36$ This depressed feature suggests that the equivalent circuit is formed by a distribution of parallel resistance and capacitor circuits rather than being defined by a single circuit. Such a distribution is generated by the disorder due to size and position fluctuations of the nanoparticles and also to point defects and dislocations present in the assembly network (Figure 2a and Figure ESI 1a). Indeed, as shown in Figure ESI 4, for a perfectly ordered hexagonal arrangement of the nanoparticles, the calculated Nyquist plot is a perfect semi-circle. When 15% random fluctuations of the nanoparticle size and position are introduced, all the Nyquist plots calculated for the different random guesses, are not only depressed but their shape clearly deviates from a semi-circle (Figure ESI 4). This occurs because of the fluctuations of the local inter-particle tunneling resistance R_{ij}, capacitor C_{ij} and photo-conductance g_{ij_photo} which lead to statistical distributions of relaxation times $\tau_{ij} = \frac{R_{ij}C_{ij}}{1+R_{ij}g_{ij\_photo}}$. As a matter of fact, in a perfectly ordered network, the interparticle separation l_{ij} and hence R_{ij} , C_{ij} and $g_{ij\_photo}^{-1}$ are well defined, thus leading to a unique relaxation time τ_{ij} (Figure ESI 5b).

Figure 4b shows the imaginary part $-Z''$ of the impedance as a function of frequency. Each spectrum consists of a resonance peak. Assuming a perfectly ordered network, the $-Z''(\omega)$ resonance peak has a Lorentzian line shape (corresponding to a single relaxation time) and the resonance frequency is given by $f_0 = \frac{1}{2\pi RC}$; at the nano-junction scale f_0 is determined by the interparticle tunnelling resistance (Eq. 2) and capacitor (Eq. 5). In the numerical simulations, the tunnelling parameter $R_0 =$

$80\ k\Omega$ has been chosen in such a way that the resonance frequency $f_0 = 28\ kHz$ corresponds to the one observed experimentally (see discussion below), without optical excitation, which leads to $R = 1.4\ T\Omega$ and $C = 4aF$. This latter value is the equivalent capacitor of all serie and parallel nano-junctions forming the electrical network (C_{ij} being given by Eq. 5). The large value of *R* and the small value of *C* are consistent with the small size of the model nanoparticle network (100 nm x 100 nm). Under optical illumination, the resonance frequency increases with increasing light intensity (inset of Figure 4b). As a matter of fact, the resonance frequency of the equivalent circuit shown in Figure 1b is given by:

Eq. 9 $$f_0 = \frac{1+RG_{photo}}{2\pi RC}$$

Hence, when G_{photo} increases, the resistive component of the equivalent circuit decreases and the resonance frequency increases linearly with irradiation intensity (inset of Figure 4b) in agreement with Eq. 6. The maximum of the resonance peak also decreases for the same reason.

It is worth to underline that the line shape of the $-Z''(\omega)$ resonance peaks in Figure 4b is not described by a Lorentzian function. Indeed, because of the disorder effects discussed above, the resonance peaks in Figure 4b are inhomogenously broadened according to the statistical distributions of the local relaxation time τ_{ij}. To confirm this point, we have calculated analytically the impedance Nyquist plot and resonance peak starting from the distribution of the relaxation times of the model nanoparticle network shown in Figure ESI 5. The depressed feature of the Nyquist plot and the non Lorentzian shape of $-Z''$ resonance are well reproduced thus confirming the role of disorder (Figure ESI 5).

4.2 Plasmoelectronic conduction paths:

For a full understanding of the optical excitation effect on the charge transport properties, it is interesting to exploit the numerical simulations in order to investigate the conduction paths supported by the nanoparticle network. The length of a conducting path and its electric characteristics are extracted from the numerical simulations as follows: first, the spatial distribution of all the nano-junctions formed by each pair of first neighbor nanoparticles is constructed according to the positions of the nanoparticles within the network. Second, only paths connecting the injection and the collection electrodes are selected. These percolating paths are the ones directly involved in the impedance spectroscopy measurements. Then, the length L_k of each individual k-path is calculated by summing the nano-junctions impedance. Its admittance is given by:

Eq. 10 : $$Y_k = \frac{\prod_{n=1}^{m} \chi_{ij,n}}{\sum_{n=1}^{m} \prod_{p=1,n\neq p}^{m} \chi_{ij,p}}$$

where *m* is the number of nano-junctions along the k-path and χ_{ij} is a nano-junction admittance (Eq. 1).

Figure 5 displays path length histograms calculated at the resonance frequency f_0= 28 kHz of the nanoparticle network. Without optical excitation, the path length histogram is bimodal with a main maximum around 220 nm, *i.e.*, nearly twice the inter-electrode separation and a secondary maximum at longer paths between 300 and 400 nm. Under optical excitation at 1 W/cm^2, the distribution of path lengths is more

uniform: the path length histogram is Gaussian like centered around 250 nm with 100 nm half width at half maximum. The optical excitation has the effect of condensing the conduction path lengths around a mean value. This is related to the fact that the photo-resistance (Eq. 6) due to the hot charge carriers is less sensitive to disorder effects (*i.e.* to nanoparticle size and position fluctuations) than the resistance associated with thermalized charge carriers (see Figure ESI 6).

Figure 5 c-f depict the real (conductance) and imaginary (susceptance) parts of path admittance as a function of path length calculated at the resonance frequency. For a given path length, the values of the admittance are scattered over a wide range (Figure 5 c-f) which means that paths of the same length may have very different electrical characteristics. This is particularly visible in the conductance (Figure 5c, d) because the tunnelling resistance varies exponentially with the inter-particle distance (Eq. 2) and is therefore very sensitive to fluctuations of the size and position of a nanoparticle within the network. The susceptance of the nanoparticle network (Figure 5e, f) is less sensitive to disorder effects because of the weaker logarithmic dependence of the local capacitors (Eq. 5) on the interparticle distance.

As shown in Figure 5c, d path admittance is enhanced by the optical excitation in agreement with Nyquist plots (Figure 4); as a consequence, for a given path length, the conductance and susceptance are scattered over a wider range (compared to Figure 5 e, f). The optical excitation has a strong impact on the conductance since the local photo-conductance introduced in Eq. 6 is purely real. For this same reason, we might have expected no influence on the susceptance. However, since the complex admittance combines both resistive and capacitive contributions (Eq. 10), its susceptance component depends not only on the local interparticle resistance R_{ij} and local interparticle capacitor C_{ij}, but also on the local photo-resistance $g_{ij\_photo}^{-1}$. That's why the susceptance of the nanoparticle network is also modified by the optical excitation. The path admittance is strongly influenced by disorder as shown by the scattered values of conductance and capacitance (Figure 5c-f) and decreases roughly as the inverse path length. They are strictly proportional to the inverse path length only in the case of a perfectly ordered network as shown in previous works [34].

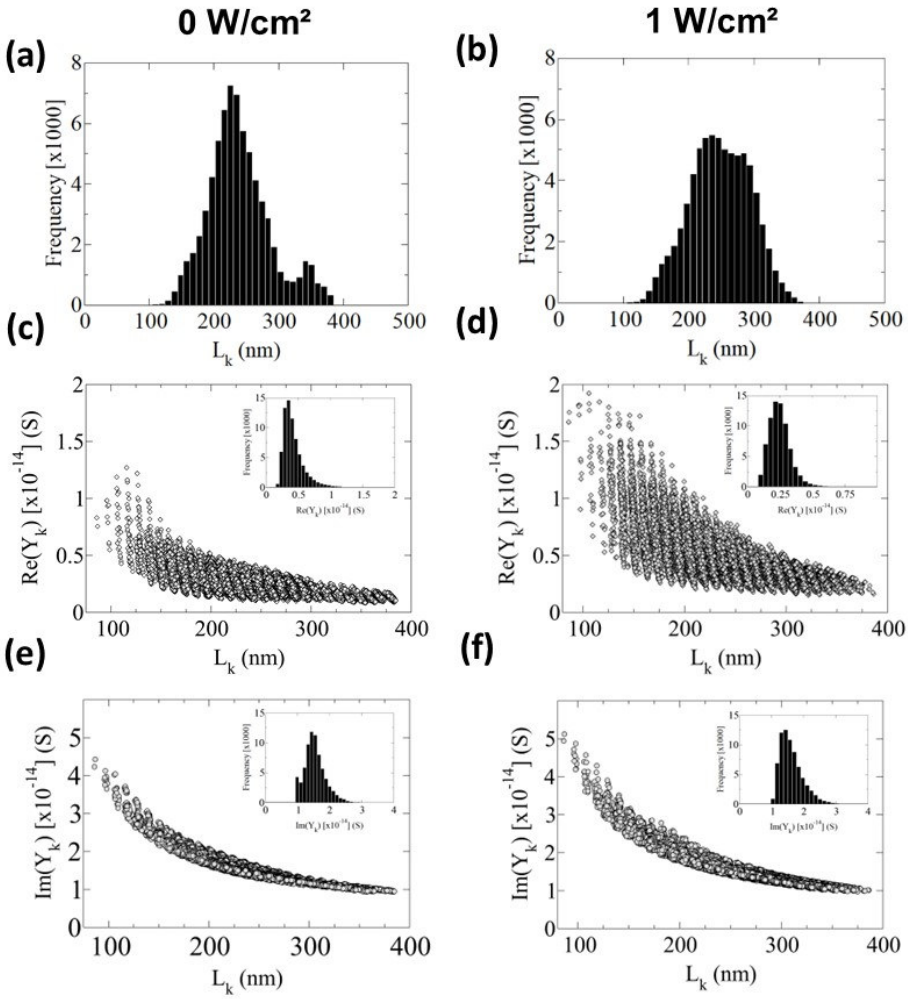

Figure 5 : (a,b) histograms of conduction path lengths extracted from the DDA-Kirchhoff numerical simulations of the TEM nanoparticle network shown in Figure ESI 1a. Calculations were performed at the resonance frequency f_0=28 kHz, without and with optical excitation at 560 nm wavelength and 1 W/cm² intensity. (c, d) path conductance as a function of path length L_k. (e, f) path susceptance as a function of path length L_k. The insets in c-f show conductance (c,d) and susceptance (e-f) histograms.

Moreover, Figure 5 c-f display the conductance and susceptance histograms calculated with and without optical excitation. The histograms follow a log-normal distribution, as shown in a previous study [34], which indicates that conductance and susceptance indeed result from the sum of the numerous small independent local interparticle impedances along the conducting paths.

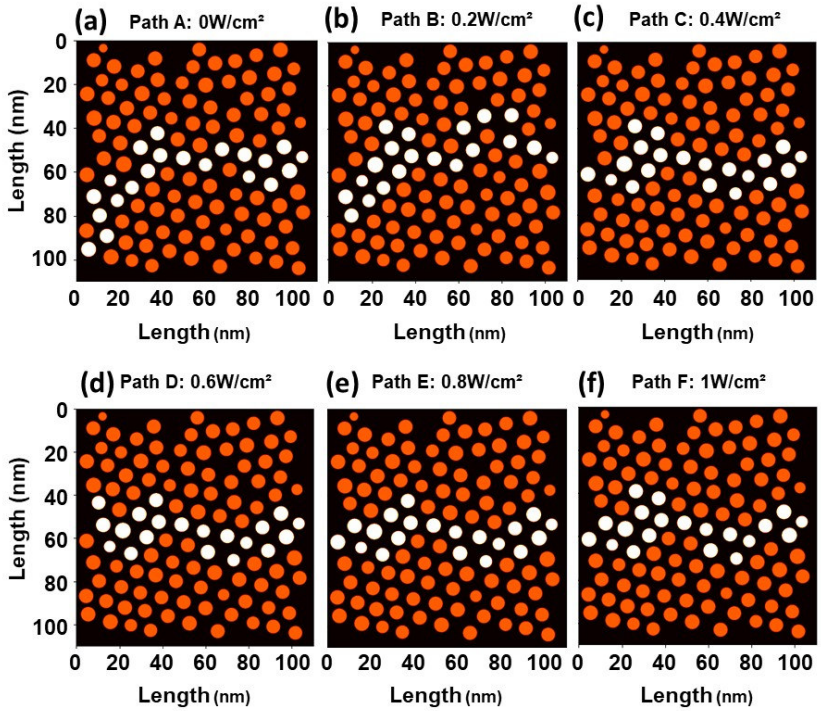

Figure 6 : Plasmo-electronic conduction paths. (a) Conduction path A is calculated without optical excitation. (b, c and d) Paths B, C and D are calculated with optical excitation at 532 nm and intensity from 0 to 1 W/cm². Each path module admittance $|Y_k|$ is in the range [1.8x10^{-14} S - 2x10^{-14} S]. The path length decreases from 200 nm for path A to 197 nm for path F.

DDA-Kirchhoff numerical simulations allow to visualize the conduction paths and the changes induced by the optical excitation. To do so, we have selected conduction paths with nearly the same conductance c.a. 2.10^{-14} S and comparable length around 200 nm, *i.e.*, twice the network size and inter-electrodes separation. In this way, when the optical excitation is applied, only the relative contribution of the resistance and photo-resistance, along the path, is modified; its overall conductance being nearly constant. Figure 6 displays such conduction paths without (path labeled A) and with (paths labeled B-F) optical excitation. Without optical excitation, path A involves 21 nano-particles and the average distance between the involved first neighbor nanoparticles is 2.68 nm. With optical excitation at a moderate intensity of 0.2W/cm^2, path B is 198 nm long and involves 20 nanoparticles with a slightly larger average interparticle distance of 2.70 nm. When the optical excitation is increased to 0.4W/cm^2, path C involves 20 nanoparticles with an average distance of 2.74 nm. With further increase from 0.6 to 1 W/cm^2, the length of path D, E and F are *c.a.* 197nm and involves 20 nanoparticles with increasing average distances from 2.78 to 2.84 nm (see Figure 7). The variation of the relative admittance $\Delta Y_k = (|Y_k|-|Y_k|_{dark})/ |Y_k|_{dark})$ of the conduction paths shown in Figure 6 is less than 5% which ensures the fact that we are comparing conduction paths with very similar admittance.

It appears that the effect of the optical excitation is to reduce the path length and correlatively increase the average distance $\langle l_{ij} \rangle$ between first neighbor

nanoparticles for a given path admittance. We found that $\langle l_{ij} \rangle$ increases by *c.a.* 0.16 nm per unit of optical excitation intensity (in $W^{-1}cm^2$) as shown in Figure 7.

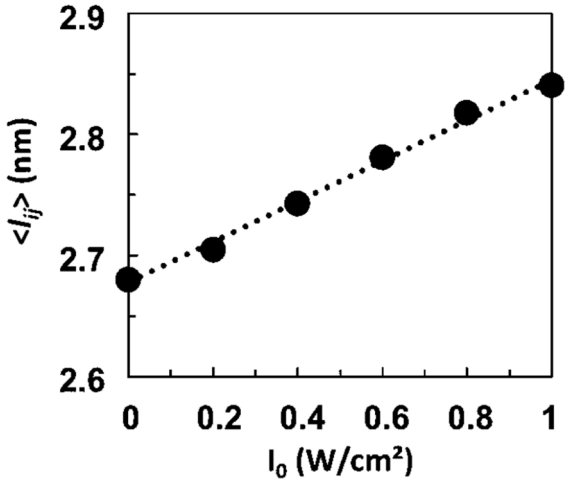

*Figure 7 : Average distance $\langle l_{ij} \rangle$ between first neighbor nanoparticles involved in the plasmoelectronic conduction p*aths (A to F of *Figure 6*) *as a function of laser intensity I_0. The doted line shows a linear least-square fit.*

This effect can be understood in terms of optical generation of hot carrier's. Indeed, according to the local photo-conductivity (Eq. 6 and Eq. 7), the photo-excited hot carriers can tunnel over larger distances ($\beta^{-1} = 0.27\,nm$) than thermalized carriers ($\beta^{-1} = 0.2\,nm$). Therefore, under optical excitation a smaller number of nanoparticles is required for a conduction path with the same conductance compared to the situation without optical excitation. This underlines the role of the plasmonic resonance in terms of not only enhancement of the local optical field (Figure 3), but also of photo-generation of hot carriers. This latter effect is at the origin of the different optical conduction paths displayed in Figure 6 which we may call plasmo-electronic conduction paths.

4.3 Comparison between DDA-Kirchhoff simulations and experiments:

One must scale-up the dimensions of the simulated nanoparticle network to the macroscopic scale in order to compare numerical simulations with impedance spectroscopy data, quantitatively. However, numerical simulations of the charge transport properties of a macroscopic nanoparticle network require a significant amount of computation time and memory resources. To overcome this difficulty we use a simple rescaling method: the 100 nm x 100 nm simulated network (Figure 1) is replicated N_i times in series and N_j times in parallel; N_i and N_j are determined, respectively, by the distance between the interdigitated electrodes (Figure 1) and by their length. Additionally, a series contact resistance R_S can be added to take into account imperfections in the electrical connexion between the electrodes and the nanoparticle network. Then, the macroscopic impedance is calculated simply as

Eq. 11
$$Z_{macro}(\omega) = R_s + \frac{1}{N_e}.\frac{N_i}{N_j}.Z(\omega)$$

where $Z(\omega)$ is the mesoscale impedance of the 100 nm x 100 nm nanoparticle network calculated by DDA-Kirchhoff numerical simulations (Figure 3) and N_e is the

number of interdigited electrodes (Figure 1). In our device N_i=50; N_j=10000 and N_e=*50*.

At high frequencies, the resistance of the nanoparticle network is shorted by its capacitance and only the series resistance R_s remains and can be estimated from the experimental data. We found $R_s \leq 1k\Omega$ from the impedance measured at the highest reachable frequency (10 MHz in our case). It is worth to underline that, according to Eq. 11, $-Z''_{macro}(\omega)$ and $-Z''(\omega)$ peaks exhibit the same resonance frequency f_0 and line shape; they differ only in their magnitudes by the scaling factor $\frac{1}{N_e}.\frac{N_i}{N_j}$. The straightforward rescaling method (Eq. 11) assumes that the size of the mesoscale network is large enough to capture all the structural features of the nanoparticle network, *i.e.*, the spatial arrangement of the nanoparticles including fluctuations of their sizes and positions as well as the presence of point defects and dislocations.

Figure 8 presents a comparison between the results of DDA-Kirchhoff's numerical simulations and impedance spectroscopy data.

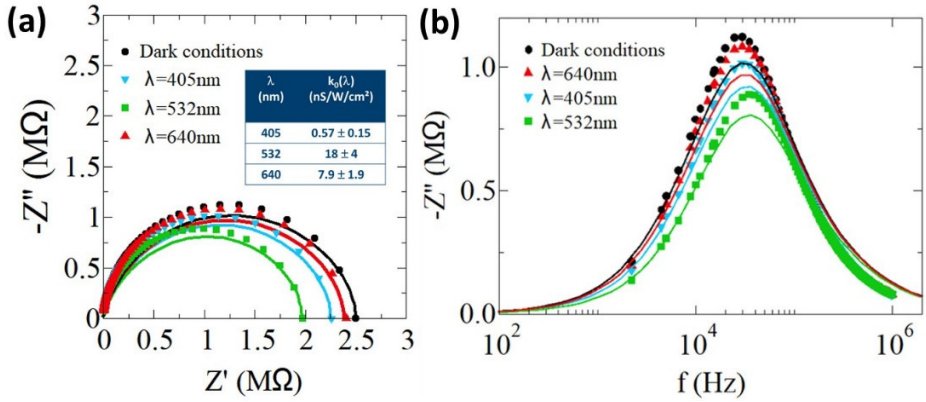

Figure 8 : (a) Comparison between measured and calculated (full lines) impedance Nyquist's plots without and with optical excitation at λ = 405, 532, 640 nm and 0.36 W/cm² intensity (b) corresponding spectra of $-Z''(\omega)$; the table inserted in (a) shows the values of the $k_0(\lambda)$ factor in Eq. 6 used as a fitting parameter of the simulated Nyquist plots to the measured ones.

In the numerical simulations there are two adjustable parameters: the interparticle tunneling resistance R_0 in Eq. 2 and the charge carrier photo-generation efficiency k_0 in Eq. 7 when the optical excitation is used. As mentioned above, $R_0 = 80\ k\Omega$ has been determined in such a way that the calculated resonance frequency $f_0 = 28\ kHz$ coincides with the one observed in the impedance spectroscopy measurements. Using this value of R_0 and the rescaling method described above one obtains the macroscopic values $R{\sim}140M\Omega$ and $C{\sim}0.04pF$. At this point one expects a good matching between the rescaled impedance (Eq. 11) and the measured one. However, we found that the calculations overestimate the measured impedance. The latter is of the order of 2.5 MΩ as can be seen on the Nyquist's plot (horizontal axis of Figure 8). The origin of this discrepancy lies in three main points:

First, the mesoscale network is assumed to be representative of the entire macroscopic network. However, Figure ESI 4 shows that for a 100 nm x 100 nm network with a hexagonal arrangement of the nanoparticles in which 15% size and position fluctuations are included, the impedance may vary up to a factor 20 depending on the network selected by the random guess (only a factor 4 is presented in Figure ESI 4).

Second, we found that depending on the filtering parameters used in the software assisted filtering of the TEM image (Figure ESI 1a), the estimated nanoparticle size position may vary by 5%. This variation, combined with the strong sensitivity of the tunneling resistance to the inter-particle distance (Eq. 2), leads to an uncertainty on the calculated network impedance that may also reach an order of magnitude. Moreover, the parameters β and E_C determine the interparticle tunneling resistance (Eq. 2) and may be affected by conformational changes of the ligand molecules which in turn may have a strong impact on the overall macroscopic resistance.

Third, we did not take into account a possible effect of humidity from the environment that would modify the conformation of the ligand molecules and thus the permittivity of the medium surrounding the nanoparticles.

For these reasons, the calculated and measured impedances are significantly different in magnitudes. However, the shape of the calculated and measured Nyquist diagrams and resonance peaks can be compared once their amplitudes adjusted. To do that, the calculated low-frequency impedance is fitted to the measured one, in the absence of optical excitation. This corresponds to the (black) dot on the right side (horizontal axis) of the Nyquist plot in Figure 8a. As shown in Figure 8, the Nyquist plot, measured without optical excitation, is depressed $-Z''_{max}/Z'_{max}\sim 0.4$ (Figure 8a and Figure ESI 6) and the resonance peak of $-Z''(\omega)$ has a non-lorentzian shape characterized by a low-frequency asymmetry. The calculations (full lines in Figure 8) well account for these two features which are correlated and reflect the disorder effects discussed in Figure 4. In fact, the measured and calculated linewidths of the resonance peaks in Figure 8b are comparable, hence indicating that the variations in the size and location of the nanoparticles and the networks defects (disorientations, dislocations…) (Figure 1) are quite representative of the disorder present at the macroscopic scale.

Let's now focus on the effect of the optical excitation. As shown in Figure 8, the nanoparticle assembly has been excited at 405, 532 and 640 nm wavelengths with 0.36 W/cm² laser intensity. The reduction in the radius of the Nyquist plots in Figure 8a and in the amplitude of the resonance peaks in Figure 8b demonstrate that, after optical excitation, the measured impedance of the nanoparticle network is lowered due to a photo-conductance contribution in agreement with the simulation results presented in Figure 4. Remarkably, the largest photo-induced effect is observed for $\lambda = 532$ nm (green dots in Figure 8a), *i.e.*, close to the plasmon resonance of the nanoparticle network (Figure 2) which underlines the plasmo-electronic character of the photo-conductance.

DDA-Kirchhoff numerical simulations of the photo-induced plasmo-electronic effect were then performed using the photo-current factor $k_0(\lambda)$ in Eq. 7 as an adjustable parameter. The agreement between the calculated and measured impedance Nyquist plots and resonance peaks, under optical excitation, is satisfactory. In particular, the depressed character (Figure 8a) of the Nyquist plots and the linewidth of the resonance peaks (*Figure 8*b) are well reproduced. The $k_0(\lambda)$ best-fit values are quoted in *Figure 8*b. Close to the plasmonic resonance the photo-current conversion factor is estimated at $k_0(532nm) = 18 \pm 4\ nS.W^{-1}.cm^2$ which means that at 0.36 W/cm², for nearly touching particles, the inter-particle photo-conductance is around 50 nS.

It is worth to underline that using the values of the nanoscopic photo-conductance efficiency $k_0(\lambda)$ quoted in Figure 8a, the DDA-Kirchhoff numerical

simulations are able to account for the measured macroscopic photo-conductance as a function of both the optical excitation wavelength (Figure 8) and intensity (Figure 9). Close to the plasmonic resonance($\lambda = 532nm$), we found that the macroscopic photo-conductance efficiency is 250 ± 40 nS.W^{-1}.cm^2.

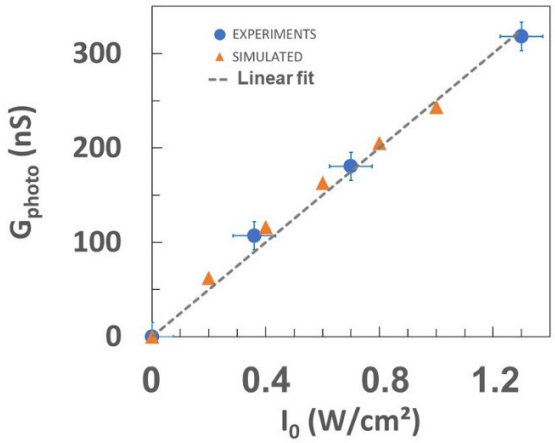

Figure 9 : Calculated (triangles) and measured (dots) macroscopic photoconductance G_{photo} as a function of laser intensity I_0 at the plasmonic resonance (λ=532nm). The experimental photoconductance is extracted from the low-frequency impedance spectroscopy measurements performed under optical excitation (Figure 8). The dashed line shows the linear variation fit which gives a macroscopic photo-conductance efficiency of 250 ± 40 nS.W^{-1}.cm^2.

As mentioned above, $k_0(\lambda)$ in Eq. 6 accounts for the light absorption and for the inter-particle charge transfer of the photo-generated charge carriers. The fact, that $k_0(\lambda)$ is maximum at $\lambda = 532\ nm$ has to do with the transition dipole between initial and final states involved in the optical absorption process. As a matter of fact, gold has inter-band transitions between occupied d-orbital and unoccupied s-orbital states (above the Fermi level) with a maximum absorption around 500 nm wavelength [35]. The inter-band transitions overlap with the plasmonic resonance which is responsible for the decay of the surface plasmons into hot electron-hole pairs. Therefore, a maximum efficiency of photo-carrier generation is expected at the plasmonic resonance as observed in Figure *8*. Moreover, hybridization between the metal nanoparticle and the dodecanethiol electronic states takes place because of the strong bonding of the thiol molecules with the metal surface. In that case, one may also expect transitions from the occupied d-orbital states of the gold nanoparticle to the un-occupied states of the thiol molecule which may also contribute to $k_0(\lambda)$. The hybridization of the molecule/nanoparticle electronic states still need to be modelled using quantum mechanics and implemented into DDA-Kirchhoff numerical simulations in order to fully account for the photo-induced effects in self-assembled nanoparticle assemblies.

5. CONCLUSION

To summarize, we presented a theoretical investigation of the plasmo-electronic properties of self-assembled gold nanoparticle networks in conjunction with impedance spectroscopy measurements. A photo-electric nano-junction model, formed by first neighbor nanoparticles, was introduced as an elementary building

block of a mesoscopic electrical circuit; the latter was rescaled to allow comparison with experiments performed at the macroscopic scale. Its electric properties (resistance, capacitance, and photo-resistance) were obtained by incorporating electro-dynamic calculations of the local optical properties, based on the DDA method, into Kirchhoff's current-bias equations. An important feature of the theoretical modeling is that the actual spatial sizes and relative positions of the nanoparticles within the self-assembly are taken into account as they determine the local resistance, capacitance and photo-resistance. The charge carrier transport across the nanoparticle network was numerically simulated using the developed DDA-Kirchhoff combined approach, and analyzed in terms of impedance Nyquist's plots and resonance properties. The effect of structural disorder has been addressed because it is critical in understanding the shape of impedance Nyquist plots and resonance curves. The DDA-Kirchhoff numerical simulations were used to determine the percolating conduction paths, their statistical distribution, and the effect of optical excitation. Our main findings are : (i) the plasmonic assisted photo-conductance is responsible for a decrease of the network admittance and impacts both its impedance and susceptance. (ii) the shapes of the impedance Nyquist plot and resonance curve may strongly deviate from, respectively, a semi-circle and a Lorentzian function because of inhomogeneous distribution of relaxation times induced by disorder effects. (iii) the histograms of length and admittance of conductions paths depend on optical excitation intensity. The path impedance and susceptance decrease roughly as the inverse path length. (iv) using quantitative comparison between DDA-Kirchhoff numerical simulations and experimental impedance spectroscopy data, the local photo-conductance of a single nano-junction, with nearly teaching nano-particles, is estimated at 18 ± 4 nS.W^{-1}.cm^2 at the plasmonic resonance. (v) using a close inspection of plasmo-electronic conduction paths, we found that the role of the plasmonic resonance is twofold : first it is responsible for enhancement of the photo-conductance through increased local optical field intensity. Second, the conversion of surface plasmons into photo-generated hot charge carriers allow for inter-particle tunneling over larger distances than thermalized ones.

The approach developed in this work is generic and can be used to account for the transduction of light into electrical current in composite materials once the local electric characteristics of the charge transport are implemented in elementary junctions forming an electrical network.

ACKNOWLEDGMENTS :

This work is dedicated to the memory of our colleague Benoit Viallet who initiated the numerical simulations of the electric characteristics of nanoparticle networks. The authors are grateful to T. Alnasser for the chemical synthesis of gold nanoparticles. This study has been supported through the EUR grant NanoX No. ANR-17-EURE-0009 in the framework of the Programme des Investissements d'Avenir. This work was performed using HPC resources from CALMIP (Grant P0996).

CONFLICT OF INTEREST:

The authors declare no conflict of interest.

DATA AVAILABILITY:

Data underlying the results presented in this paper are not publicly available at this time but may be obtained from the authors upon reasonable request.

SUPPLEMENTARY MATERIAL:

Inter-nanoparticle distance histogram, Normalized measured photoconductance G_{photo}, Schematic of inter-particle energy alignment, Impact of the network dispersion on the depressed semi-circles, Distribution of relaxation times in disordered nanoparticle networks, Impact of the laser irradiation on the depressed semi-circles.

REFERENCES :

1. K. R. Catchpole et A. Polman, « Design principles for particle plasmon enhanced solar cells », *Appl. Phys. Lett.*, vol. 93, nº 19, p. 191113, 2008, doi: 10.1063/1.3021072.
2. H. A. Atwater et A. Polman, « Plasmonics for improved photovoltaic devices », *Nat. Mater.*, vol. 9, nº 3, p. 205‑213, mars 2010, doi: 10.1038/nmat2629.
3. Jianhui Liao, Sander Blok, Sense Jan van der Molen, Sandra Diefenbach, Alexander W. Holleitner, Christian Schönenberger, Anton Vladykae and Michel Calame*, « Ordered nanoparticle arrays interconnected by molecular linkers: electronic and optoelectronic properties », *Chem Soc Rev*, vol. 44, nº 4, p. 999‑1014, 2015, doi: 10.1039/C4CS00225C.
4. Tatsuya Hashimoto, Yurie Fukunishi, Bin Zheng, Yukiharu Uraoka, Takuji Hosoi, Takayoshi Shimura, and Heiji Watanabe, « Electrical detection of surface plasmon resonance phenomena by a photoelectronic device integrated with gold nanoparticle plasmon antenna », *Appl. Phys. Lett.*, vol. 102, nº 8, p. 083702, 2013, doi: 10.1063/1.4792210.
5. P. Banerjee, D. Conklin, S. Nanayakkara, T.-H. Park, M. J. Therien, et D. A. Bonnell, « Plasmon-Induced Electrical Conduction in Molecular Devices », *ACS Nano*, vol. 4, nº 2, p. 1019‑1025, févr. 2010, doi: 10.1021/nn901148m.
6. Hideyuki Nakanishi, Kyle J. M. Bishop, Bartlomiej Kowalczyk, Abraham Nitzan, Emily A. Weiss, Konstantin V. Tretiakov, Mario M. Apodaca, Rafal Klajn, J. Fraser Stoddart & Bartosz A. Grzybowski, « Photoconductance and inverse photoconductance in films of functionalized metal nanoparticles », *Nature*, vol. 460, nº 7253, p. 371‑375, 2009.
7. Guillermo Garcia, Raffaella Buonsanti, Evan L. Runnerstrom, Rueben J. Mendelsberg, Anna Llordes, Andre Anders, Thomas J. Richardson, and Delia J. Milliron, « Dynamically Modulating the Surface Plasmon Resonance of Doped Semiconductor Nanocrystals », *Nano Lett.*, vol. 11, nº 10, p. 4415‑4420, oct. 2011, doi: 10.1021/nl202597n.
8. S. C. Warren, D. A. Walker, et B. A. Grzybowski, « Plasmoelectronics: Coupling Plasmonic Excitation with Electron Flow », *Langmuir*, vol. 28, nº 24, p. 9093‑9102, juin 2012, doi: 10.1021/la300377j.
9. M. A. Mangold, C. Weiss, M. Calame, et A. W. Holleitner, « Surface plasmon enhanced photoconductance of gold nanoparticle arrays with incorporated alkane linkers », *Appl. Phys. Lett.*, vol. 94, nº 16, p. 161104, 2009, doi: 10.1063/1.3116148.
10. M. A. Mangold, M. Calame, M. Mayor, et A. W. Holleitner, « Resonant Photoconductance of Molecular Junctions Formed in Gold Nanoparticle Arrays », *J. Am. Chem. Soc.*, vol. 133, nº 31, p. 12185‑12191, août 2011, doi: 10.1021/ja204240v.
11. J. Grisolia, N. Decorde, M. Gauvin, N. M. Sangeetha, B. Viallet, et L. Ressier, « Electron transport within transparent assemblies of tin-doped indium oxide colloidal nanocrystals », *Nanotechnology*, vol. 26, nº 33, p. 335702, juill. 2015, doi: 10.1088/0957-4484/26/33/335702.
12. H. Nesser, J. Grisolia,*, A. Mlayah, T. Alnasser, D. Lagarde, B. Viallet, L. Ressier, « Plasmonic photocapacitance of self-assembled gold colloidal nanoparticle monolayers », *Mater. Today Nano*, vol. 4, p. 38‑45, déc. 2018, doi: 10.1016/j.mtnano.2018.12.001.
13. Nicolas Decorde, Neralagatta M. Sangeetha, Benoit Viallet, Guillaume Viau, Jérémie Grisolia, Alessandro Coati, Alina Vlad, Yves Garreau and Laurence Ressier*, « Small angle X-ray scattering coupled with in situ electromechanical probing of nanoparticle-based resistive strain gauges », *Nanoscale*, vol. 6, nº 24, p. 15107‑15116, 2014, doi: 10.1039/C4NR04129A.
14. Helena Moreira, Jérémie Grisolia, Neralagatta M Sangeetha, Nicolas Decorde, Cosmin Farcau, Benoit Viallet, Ke Chen, Guillaume Viau and Laurence Ressier, « Electron transport in gold colloidal nanoparticle-based strain gauges. », *Nanotechnology*, vol. 24, nº 9, p. 095701, mars 2013, doi: 10.1088/0957-4484/24/9/095701.
15. K. E. Mueggenburg, X.-M. Lin, R. H. Goldsmith, et H. M. Jaeger, « Elastic membranes of close-packed nanoparticle arrays. », *Nat. Mater.*, vol. 6, nº 9, p. 656‑660, sept. 2007, doi: 10.1038/nmat1965.
16. J. Liao, Y. Zhou, C. Huang, Y. Wang, et L. Peng, « Fabrication, Transfer, and Transport Properties of Monolayered Freestanding Nanoparticle Sheets », *Small*, vol. 7, nº 5, p. 583‑587, 2011, doi: https://doi.org/10.1002/smll.201002078.
17. M. A. Mangold, M. Calame, M. Mayor, et A. W. Holleitner, « Negative differential photoconductance in gold nanoparticle arrays in the Coulomb blockade regime », *ACS Nano*, vol. 6, nº 5, p. 4181—4189, mai 2012, doi: 10.1021/nn300673t.
18. I. S. Beloborodov, A. V. Lopatin, V. M. Vinokur, et K. B. Efetov, « Granular electronic systems », *Rev Mod Phys*, vol. 79, nº 2, p. 469‑518, avr. 2007, doi: 10.1103/RevModPhys.79.469.
19. J. Herrmann, K.-H. Müller, T. Reda, G. R. Baxter, B. Raguse, G. J. J. B. de Groot, R. Chai, M. Roberts, and L. Wieczorek, « Nanoparticle films as sensitive strain gauges », *Appl. Phys. Lett.*, vol. 91, nº 18, p. 183105, 2007, doi: 10.1063/1.2805026.

20. Roger H. Terrill, Timothy A. Postlethwaite, Chun-hsien Chen, Chi-Duen Poon, Andreas Terzis, Aid Chen, James E. Hutchison,Michael R. Clark, George Wignall, Juan D. Londono, Richard Superfine, Mike Falvo, Charles S. Johnson Jr., Edward T. Samulski, and Royce W. Murray, « Monolayers in Three Dimensions: NMR, SAXS, Thermal, and Electron Hopping Studies of Alkanethiol Stabilized Gold Clusters », *J. Am. Chem. Soc.*, vol. 117, nº 50, p. 12537‑12548, déc. 1995, doi: 10.1021/ja00155a017.
21. T. Vossmeyer, C. Stolte, M. Ijeh, A. Kornowski, et H. Weller, « Networked Gold-Nanoparticle Coatings on Polyethylene: Charge Transport and Strain Sensitivity », *Adv. Funct. Mater.*, vol. 18, nº 11, p. 1611‑1616, juin 2008, doi: 10.1002/adfm.200701509.
22. H. Nesser, J. Grisolia, T. Alnasser, B. Viallet, et L. Ressier, « Towards wireless highly sensitive capacitive strain sensors based on gold colloidal nanoparticles », *Nanoscale*, vol. 10, nº 22, p. 10479‑10487, 2018, doi: 10.1039/C7NR09685B.
23. M. Gauvin, J. Grisolia, T. Alnasser, B. Viallet, S. Xie, J. Brugger and L. Ressier*, « Electro-mechanical sensing in freestanding monolayered gold nanoparticle membranes », *Nanoscale*, vol. 8, nº 22, p. 11363‑11370, 2016, doi: 10.1039/C6NR02004F.
24. N. Zheng, J. Fan, et G. D. Stucky, « One-Step One-Phase Synthesis of Monodisperse Noble-Metallic Nanoparticles and Their Colloidal Crystals », *J. Am. Chem. Soc.*, vol. 128, nº 20, p. 6550‑6551, mai 2006, doi: 10.1021/ja0604717.
25. M. M. A. Yajadda, K.-H. Müller, et K. Ostrikov, « Effect of Coulomb blockade, gold resistance, and thermal expansion on the electrical resistance of ultrathin gold films », *Phys Rev B*, vol. 84, nº 23, p. 235431, déc. 2011, doi: 10.1103/PhysRevB.84.235431.
26. Aidan J. Quinn Dr., Paul Beecher Dr., Daniela Iacopino Dr., Liam Floyd, Gianluca De Marzi Dr., Elena V. Shevchenko Dr., Horst Weller Prof. Dr., Gareth Redmond Dr, « Manipulating the charging energy of nanocrystal arrays. », *Small Weinh. Bergstr. Ger.*, vol. 1, nº 6, p. 613‑618, juin 2005, doi: 10.1002/smll.200500057.
27. K.-H. Müller et M. M. A. Yajadda, « Electron transport in discontinuous gold films and the effect of Coulomb blockade and percolation », *J. Appl. Phys.*, vol. 111, nº 12, p. 123705, 2012, doi: 10.1063/1.4729491.
28. M. Gauvin, T. Alnasser, E. Terver, I. Abid, A. Mlayah, S. Xie, J. Brugger, B. Viallet, L. Ressier and J. Grisolia*, « Plasmonic photo-current in freestanding monolayered gold nanoparticle membranes », *Nanoscale*, vol. 8, nº 36, p. 16162‑16167, 2016, doi: 10.1039/C6NR05091C.
29. Hylke B. Akkerman, Ronald C. G. Naber, Bert Jongbloed, Paul A. van Hal, Paul W. M. Blom, Dago M. de Leeuw, and Bert de Boer, « Electron tunneling through alkanedithiol self-assembled monolayers in large-area molecular junctions », *Proc. Natl. Acad. Sci.*, vol. 104, nº 27, p. 11161‑11166, 2007, doi: 10.1073/pnas.0701472104.
30. B. T. Draine et P. J. Flatau, « Discrete-Dipole Approximation For Scattering Calculations », *J Opt Soc Am A*, vol. 11, nº 4, p. 1491‑1499, avr. 1994, doi: 10.1364/JOSAA.11.001491.
31. B. T. Draine et P. J. Flatau, « Discrete-dipole approximation for periodic targets: theory and tests », *J Opt Soc Am A*, vol. 25, nº 11, p. 2693‑2703, nov. 2008, doi: 10.1364/JOSAA.25.002693.
32. *Scilab, « Copyright © 1989-2005. INRIA ENPC. » and « Scilab is a trademark of INRIA ». « www.scilab.org »*. En ligne.. Disponible sur: www.scilab.org
33. P. Lagonotte et Y. Eichenlaub, « Réseaux électrocinétiques et algèbre linéaire (notions fondamentales) ». J3eA, 2005.
34. L. Merle, Delpoux, A. Mlayah, J. Grisolia, « Multiscale modeling of the dynamical conductivity of self-assembled nanoparticle networks: Numerical simulations vs analytical models »,. J. Appl. Phys. 132, 000000 (2022); [En ligne].. Disponible sur: doi: 10.1063/5.0097997
35. P. G. Etchegoin, E. C. Le Ru, et M. Meyer, « An analytic model for the optical properties of gold », *J. Chem. Phys.*, vol. 125, nº 16, p. 164705, 2006, doi: 10.1063/1.2360270.